PCCP

ROYAL SOCIETY OF CHEMISTRY

PAPER

View Article Online
View Journal | View Issue

Cite this: *Phys. Chem. Chem. Phys.*, 2021, **23**, 10218

Ultra-thin structures of manganese fluorides: conversion from manganese dichalcogenides by fluorination

Mehmet Baskurt, [a] Rahul R. Nair,[bcd] Francois M. Peeters[e] and Hasan Sahin *[a]

Received 21st January 2021,
Accepted 13th April 2021

DOI: 10.1039/d1cp00293g

rsc.li/pccp

In this study, it is predicted by density functional theory calculations that graphene-like novel ultra-thin phases of manganese fluoride crystals, that have nonlayered structures in their bulk form, can be stabilized by fluorination of manganese dichalcogenide crystals. First, it is shown that substitution of fluorine atoms with chalcogens in the manganese dichalcogenide host lattice is favorable. Among possible crystal formations, three stable ultra-thin structures of manganese fluoride, 1H-MnF_2, 1T-MnF_2 and MnF_3, are found to be stable by total energy optimization calculations. In addition, phonon calculations and Raman activity analysis reveal that predicted novel single-layers are dynamically stable crystal structures displaying distinctive characteristic peaks in their vibrational spectrum enabling experimental determination of the corresponding phases. Differing from 1H-MnF_2 antiferromagnetic (AFM) large gap semiconductor, 1T-MnF_2 and MnF_3 single-layers are semiconductors with ferromagnetic (FM) ground state.

Various experimental methods have been used in the last two decades in order to synthesize two-dimensional (2D) ultra-thin materials. Among those methods, micromechanical cleavage has been reported to be a simple and effective method for obtaining monolayers of layered bulk crystals *via* exfoliation using an adhesive tape.[1–3] In addition, chemical vapor deposition (CVD) and molecular beam epitaxy (MBE) techniques have often been used in order to produce large-scale, high-quality ultra-thin structures. However, these procedures are much less cost-effective, often intricate, and expensive.[4–8] Therefore, due to its simplicity micromechanical cleavage has been still widely used with the required improvements made for obtaining large-scale flakes.[9] Although it is a widely-used method, application of cleavage technique has been limited to crystal structures composed of van der Waals (vdW) coupled layers, and therefore, synthesis of 2D crystals from non-layered bulk structures is an important issue. Very recently, we demonstrated a novel method for the synthesis of 2D ultra-thin structures from non-layered bulk materials using the chemical conversion process.[10] It was demonstrated that for sufficiently long fluorination time, layered InSe can be turned into a thin InF_3 crystal in which all Se atoms are chemically exchanged with F atoms. It was also theoretically predicted that the fluorinated InSe is a direct band gap semiconductor and have a slightly softer crystal structure with a strong in-plane anisotropy.[11] Additionally, fluorination dependent enhancement in the stability of 2D crystals has also been reported recently.[12] Studies on chemically functionalized or converted ultra-thin crystal structures are still continuing.

Among the fluoride crystals, manganese fluorides having diverse phases have been widely used in various applications. MnF_4 is known as a powerful oxidizing agent with blue-violet color and is synthesized *via* the reaction of MnF_3 with HF.[13] It was demonstrated that MnF_3 is an effective fluorination agent which is used to convert hydrocarbons into fluorocarbons.[14] It was also reported that MnF_3 is a spin-polarized Dirac material[15] exhibiting the Jahn–Teller type distortion.[16] On the other hand, MnF_2 has also been used as an anode material in lithium-ion battery[17,18] and glass applications.[19,20] Short luminescence[21] and two-color photoluminescense[22] features of MnF_2 were also reported. Although, thin-films of manganese fluoride crystals have been studied, their ultra-thin two-dimensional structures have not been reported yet.

The research on two-dimensional ultra-thin materials has been growing exponentially since the successful isolation of graphene.[23,24] Following graphene, ultra-thin forms of other layered structures such as transition metal dichalcogenides (TMDs),[25–28] InSe,[29] and magnetic single-layers such as CrI_3,[30] VI_3,[31–33] $MnSe_2$[34] have been added to the 2D library of materials.

[a] *Department of Photonics, Izmir Institute of Technology, 35430, Izmir, Turkey. E-mail: hasansahin@iyte.edu.tr*
[b] *National Graphene Institute, University of Manchester, Manchester M13 9PL, UK*
[c] *School of Chemical Engineering and Analytical Science, University of Manchester, Manchester M13 9PL, UK*
[d] *Henry Royce Institute for Advanced Materials, Oxford Road, Manchester M13 9PL, UK*
[e] *Department of Physics, University of Antwerp, Groenenborgerlaan 171, B-2020 Antwerp, Belgium*

Magnetic single-layers are currently being used in spintronic applications however, the number of known 2D magnets is limited. Therefore, the search for novel 2D magnetic single-layers is still a hot topic in material science.

In this study, we propose the formation of different MnF_x single-layers that can be obtained through fluorination of manganese dichalcogenide structures. Our first-principles calculations reveal that the chemical exchange of F-chalcogen is energetically favorable and 1H and 1T phases of MnF_2 are formed as dynamically stable, magnetic semiconductors. In addition, ultra-thin MnF_3 is shown to be a stable magnetic semiconductor exhibiting different atomic compositions. Electronic band structure calculations indicate the formation of semiconducting MnF_xs which also exhibit distinctive vibrational properties. Thus, the chemical conversion of layered materials through fluorination can be an efficient way to obtain 2D forms of non-layered materials.

1 Computational methodology

First-principles calculations within density functional theory (DFT) were carried out in order to determine the structural, vibrational and electronic properties of single-layer MnF_x crystals by using Vienna *ab-initio* Simulation Package (VASP)[35,36] with the implemented plane-wave projector-augmented wave (PAW)[37] potentials. For the exchange–correlation functional, the generalized gradient approximation (GGA) of Perdew–Burke–Ernzerhof (PBE)[38] was used. DFT+U in Dudarev's formulation is used in order to take into account the strong correlations between the d orbitals of Mn atoms.[39] Effective parameter, U_{eff}, is taken as 3.9 eV.[40] The van der Waals correction was implemented by using the DFT-D3 method with Becke–Jonson damping.[41] The kinetic energy cut-off of the plane-wave basis set was taken to be 500 eV in all calculations. Total energy difference of 10^{-5} eV between consequent steps was taken as convergence criteria. Gaussian smearing of 0.05 eV was set for the density of states (DOS) calculations. At least 20 Å of vacuum spacing was taken in all calculations in order to prevent any interactions between adjacent layers. Γ centered k-point mesh for the primitive cell with the size of $5 \times 5 \times 1$ was used for calculating structural and vibrational properties and $8 \times 8 \times 1$ was used for density of states (DOS) calculations. Geometric relaxation of atoms was allowed until pressures in all directions became less than 1 kB. The vibrational properties of the structure were investigated by the small-displacement method.[42] The charge transfer analysis was carried out from the effective charge difference on individual atoms using the Bader technique.[43]

In order to calculate the first-order Raman activities, firstly the phonon modes at Γ point are calculated. Dynamical matrix is constructed by the results of small displacement of each atom in the unit cell. Phonon modes are obtained and the change in dielectric tensor is calculated in order to determine the corresponding Raman activity.[44,45] Raman tensor, R, is calculated by

$$R = \begin{bmatrix} \frac{\partial \alpha_{11}}{\partial Q_k} & \frac{\partial \alpha_{12}}{\partial Q_k} & \frac{\partial \alpha_{13}}{\partial Q_k} \\ \frac{\partial \alpha_{21}}{\partial Q_k} & \frac{\partial \alpha_{22}}{\partial Q_k} & \frac{\partial \alpha_{23}}{\partial Q_k} \\ \frac{\partial \alpha_{31}}{\partial Q_k} & \frac{\partial \alpha_{32}}{\partial Q_k} & \frac{\partial \alpha_{33}}{\partial Q_k} \end{bmatrix} \quad (1)$$

where Q_k is the normal mode that describes the whole motion of involving atoms of the kth phonon mode and α_{ij} is the polarizability tensor of the material. Raman activities are calculated by the equation;

$$R_A = 45\alpha^2 + 7\beta^2 \quad (2)$$

where α is the isotropic and β is the unisotropic part of the derivative of the polarizability tensor.

2 Fluorination and atomic structure

Manganese dichalcogenides, MnX_2 (X = S, Se, or Te) are known to be dynamically stable, with magnetic single-layers which exhibit layered crystal structure in their bulk forms. However, the metallic nature of MnS_2, $MnSe_2$, and $MnTe_2$ limits their use in optoelectronic device applications.[46–48] As previously achieved in InSe,[10] one can expect that the chemical conversion of these ultra-thin crystals can lead to the formation of manganese-based novel structures with new functionalities (Table 1).

The schematic representation of fluorination of MnX_2 by single fluorine atoms is shown in Fig. 1(a). Our results show that the chemical substitution of a chalcogenide atom by a F atom is energetically feasible with calculated exchange energies of −0.05, −0.29, and −1.49 eV for S, Se, and Te, respectively. Following the investigation of the energetics of single F exchange in single-layer MnX_2 structures, formation of possible MnF_2 phases with different compositions, namely 1H-MnF_2, 1T-MnF_2, and MnF_3, are examined (see in Fig. 1(b–d)).

Total energy optimization calculations show that single-layer MnF_2 structures can be crystallized either in 1H or 1T phases. In both phases, the Mn layer is sandwiched between two F layers, exhibiting $P6/m2$ and $P3/m2$ space-group symmetries, respectively.

Table 1 Calculated parameters for single-layer MnF_xs: optimized in-plane lattice constants (a and b), bond length between Mn and F (d_{Mn-F}), the F–Mn–F bond angle (θ), magnetic ground state of the structure, in-plane stiffness (C_x and C_y), the Poisson ratio (ν_x and ν_y), donated electron per Mn (ρ_{Mn}), cohesive energy per atom (E_c), work function (Φ), energy band gaps calculated within GGA (E_{gap}^{GGA}), Raman active modes

	a (Å)	b (Å)	θ (°)	Mag. state	C_x, C_y (N m^{-1})	ν_x, ν_y	ρ_{Mn} (e$^-$)	E_c (eV)	Φ (eV)	E_{gap}^{GGA} (eV)	R-Active modes (cm^{-1})
1H-MnF_2	6.26	6.26	67	AFM	57, 57	0.24, 0.24	1.5	4.31	8.54	3.82	245, 418, 447
1T-MnF_2	6.71	6.71	79	FM	47, 47	0.34, 0.34	1.6	4.52	6.96	3.67	253, 325
MnF_3	8.53	5.38	84–92	FM	40, 49	−0.46, −0.57	2.0	3.86	9.48	0.47	437, 482, 674, 1221

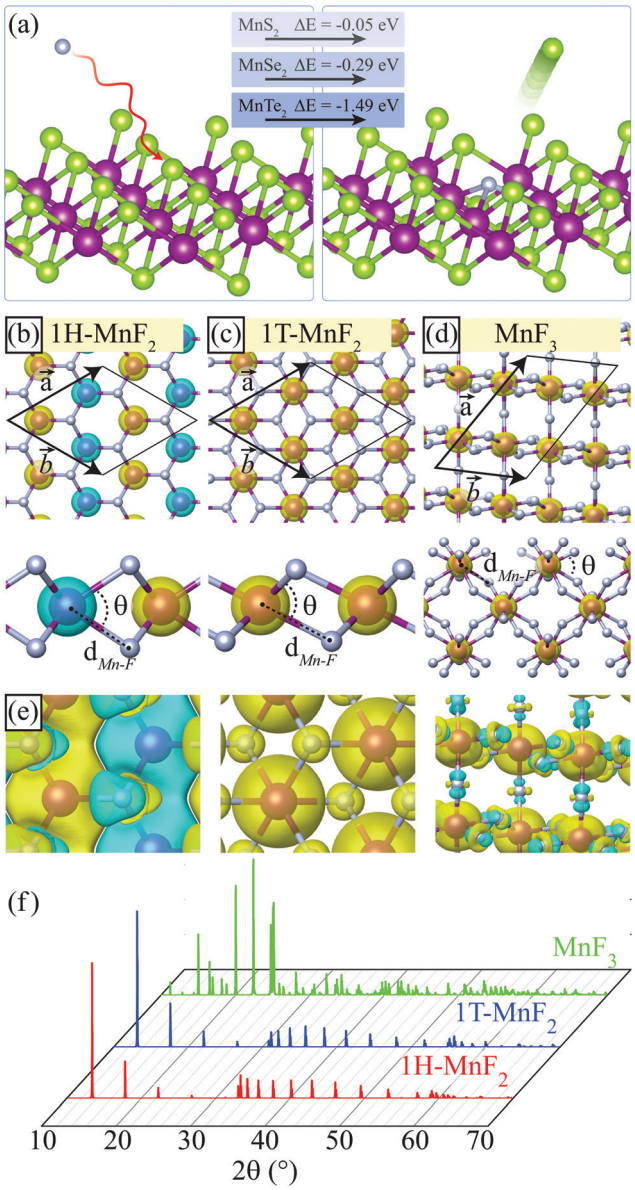

Fig. 1 (a) Schematic of the fluorination process of $MnSe_2$ monolayer with the energy difference of corresponding states given in the inset. Crystal structures with difference charge densities of (b) 1H-MnF_2, (c) 1T-MnF_2, and (d) MnF_3. (e) Superexchange interactions and (f) corresponding XRD spectra of single-layer MnF_x structures represented by red, blue and green lines, respectively. Purple, green, and violet colored atoms represent Mn, chalchogen (S, Se, Te), and F atoms, respectively.

On the other hand, single-layer MnF_3 is formed such that the Mn atoms are surrounded by bi-pyramidal tetrahedrally oriented F atoms in an accordion-like confirmation. It is calculated that in these crystal structures each Mn atom has 5 μ_B net magnetic moment. While antiferromagnetic (AFM) order is favorable for 1H phase, 1T phase favors ferromagnetic (FM) order. In addition, FM ordered state is also ground state for MnF_3 (with 4 and 3 μ_B net magnetic moment per inner and outer Mn atoms, respectively). As shown in Fig. 1 AFM (FM) order of Mn atoms in 1H-MnF_2 phase (in 1T-MnF_2 and MnF_3 phases) is stabilized by superexchange interaction provided by fluorine atoms. In addition, cohesive energies of 1H-MnF_2, 1T-MnF_2 and MnF_3 are calculated to be 4.31, 4.52 and 3.86 eV per atom, respectively. It appears that though cohesive energies of predicted single-layers are energetically less favorable than their bulk forms (4.93 and 4.56 for MnF_2 and MnF_3, respectively), their synthesis can be achieved through fluorination of ultra-thin manganese dichalcogenides.

3 Mechanical and vibrational properties

Linear-elastic properties of MnF_x single-layers are also determined in terms of the in-plane stiffness, and Poisson ratio. In-plane stiffness, $C_{x(y)}$, is the rigidity of a material while Poisson ratio, $\nu_{x(y)}$, is the ratio of transverse contraction strain to longitudinal extension. In order to determine the elastic properties of the MnF_x single-layers, elastic strain tensor elements, C_{ij} are calculated. In-plane stiffness and Poisson ratio are calculated by using the formula;

$$C_{x(y)} = \frac{(C_{11}C_{22} - C_{12} \times C_{21})}{C_{22(11)}} \quad (3)$$

$$V_{x(y)} = \frac{C_{12}}{C_{22(11)}} \quad (4)$$

In-plane stiffness values are calculated as 57 N m^{-1} for 1H-MnF_2, and 47 N m^{-1} for 1T-MnF_2. In the case of MnF_3, an in-plane anisotropy in x and y directions is predicted where the C_x and C_y values are found to be 40 and 49 N m^{-1}, respectively. As compared to the elastic constants of well-known single-layers such as graphene (330 N m^{-1}),[49,50] MoS_2 (122 N m^{-1}),[49,50] h-BN (273 N m^{-1}),[49,50] and WS_2 (122 N m^{-1}),[50] in-plane stiffness values of MnF_x single-layers indicate their ultra-soft nature. On the other hand, negative Poisson ratio values of the MnF_3 (ν_x = −0.46, ν_x = −0.57) single-layer indicate its the auxetic nature. Such materials have been used in multimodal sensing surfaces,[51] foam sensors,[52] membrane[53] and filter applications.[54] Therefore, differing from 1H and 1T structures, single-layer of MnF_3 is expected to undergo lateral expansion when stretched longitudinally and become thinner when compressed laterally.

Dynamical stability and vibrational properties of the predicted MnF_x structures are investigated in terms of their phonon band dispersions and Raman activity spectra. As presented in Fig. 2, 1H-MnF_2, 1T-MnF_2, and MnF_3 single-layers have phonon branches all having positive eigenfrequencies in the whole Brillouin zone and therefore, they are dynamically stable in free-standing form. 1H and 1T MnF_2 are found to exhibit six optical phonon branches two of which arise from the non-degenerate out-of-plane vibration of the atoms. The remaining four branches stand for in-plane vibrational motions. In the case of 1H-MnF_2, three existing Raman active modes which are named as A_1, E′, and E″ are shown in Fig. 2. The A_1 mode represents the vibration of only F atoms against each other in the out-of-plane direction while the E′ mode stands for the in-plane vibration of Mn and F atoms against each other. In addition, E″ mode arises

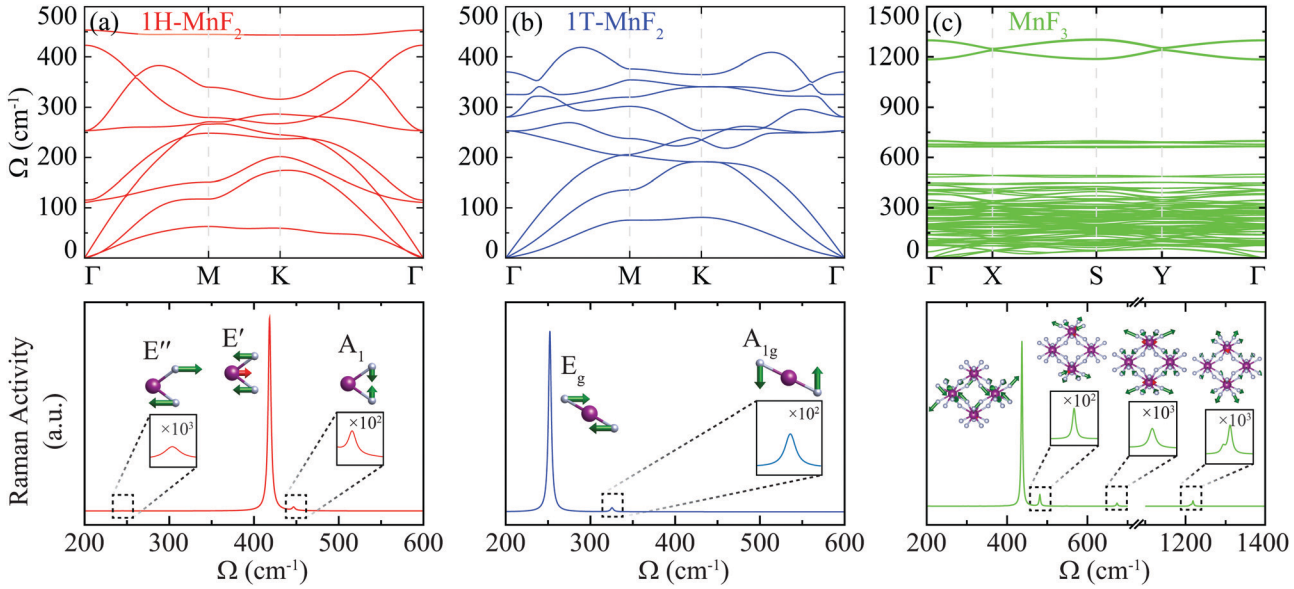

Fig. 2 Phonon dispersions and corresponding Raman spectrum of (a) 1H-MnF_2, (b) 1T-MnF_2, and (c) MnF_3.

from the opposite in-plane vibration of F atoms. On the other hand, 1T-MnF_2 exhibits two Raman active modes, namely A_{1g} and E_g. A_{1g} denotes the opposite vibration of F atoms in the out-of-plane direction while E_g represents the vibrations of F atoms against each other in the lateral directions. In the case of single-layer MnF_3, the prominent peaks in the Raman spectrum are located at 437, 482, 674, and 1221 cm^{-1} in its magnetic ground state. The most intense peak at frequency 437 cm^{-1} is attributed to the coupled in-plane and out-of-plane vibration of F atoms in the inner MnF_6 units while the other three Raman modes are dominated by the F vibrations in the outer MnF_6. While the modes at 482 and 674 cm^{-1} arise from the coupled in-plane and out-of-plane vibrations, the mode having frequency 1221 cm^{-1} is dominated by the out-of-plane vibration of the F atoms in outer MnF_6 units. Raman activity calculations, shown in lower panel of Fig. 2, reveal that for each predicted MnF_x single layer structure there are distinctive Raman-active phonon peaks and therefore, these crystal structures can be distinguished by Raman spectroscopy.

In addition to the dynamical stability, thermal stability of manganese fluoride single-layers at room temperature are investigated by performing molecular dynamics simulations. Simulations are carried out for ~2 ps with 2 fs difference between consequent steps using *NVE* ensemble. In addition, $3 \times 3 \times 1$ *k*-point sampling was chosen for $4 \times 4 \times 1$ supercell. Here, average bond length between the bonding Mn and F atoms is calculated for each time step by the equation;

$$\bar{d}_{\mathrm{Mn-F}} = \left[\sum_{i}^{n_{\mathrm{Mn}}}\sum_{j}^{n_{\mathrm{F}}}\sqrt{(x_i-x_j)^2+(y_i-y_j)^2+(z_i-z_j)^2}\Big/ n_{\mathrm{bonds(Mn-F)}}\right] \quad (5)$$

where n_{Mn} is the number of Mn atoms, n_{F} is the number of F atoms bonding with *i*th Mn atom, *i* and *j* are the indeces of Mn and F atoms, $x_{i(j)}$, $y_{i(j)}$, $z_{i(j)}$ are the coordinates of the bonding Mn and F atoms, and $n_{\mathrm{bonds(Mn-F)}}$ is the total number of Mn–F bonds. Moreover, in order to further check the stability, the average change in the atomic coordinates are calculated;

$$\Delta d = \left[\sum_{k}^{n_{\mathrm{total}}}\sqrt{(x_0-x_k)^2+(y_0-y_k)^2+(z_0-z_k)^2}\Big/ n_{\mathrm{total}}\right] \quad (6)$$

where n_{total} is the total number of atoms in the unit cell, x_0, y_0, z_0 are the coordinates of the atoms in the optimized structure, x_k, y_k, z_k are the coordinates of the *k*th atom.

It is apparently seen that, while 1T-MnF_2 and MnF_3 retain their stable phase, significant deformation occurs in the 1H-MnF_3 lattice (see Fig. 2(a and c)). For further investigation of the deformation of 1H-MnF_2, MD simulations are carried out with

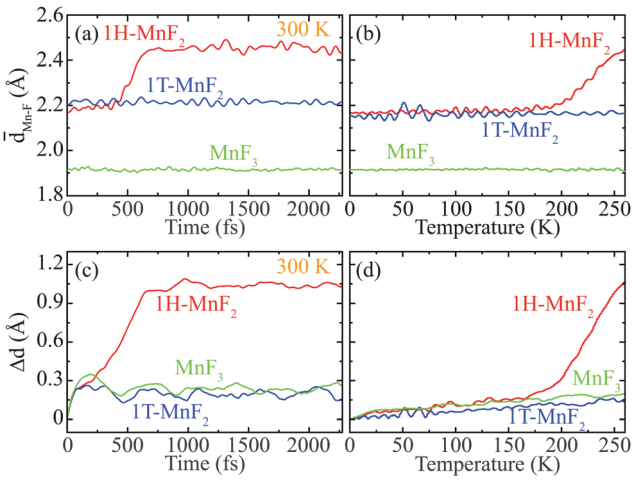

Fig. 3 Average Mn–F bond lengths in the MD simulations at (a) 300 K constant temperature, (b) rising temperature, and average atomic displacements at (c) 300 K constant temperature, (d) rising temperature.

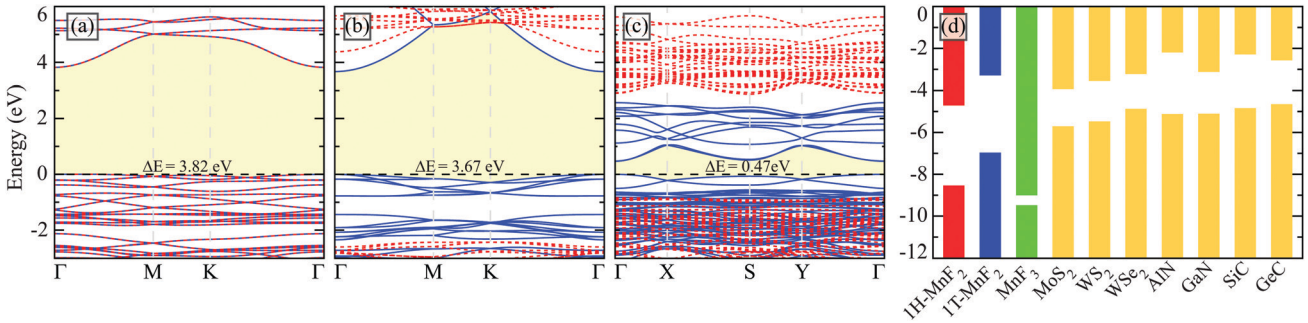

Fig. 4 Electronic band structure of (a) 1H-MnF_2, (b) 1T-MnF_2, and (c) MnF_3. Major and minor spin components are represented by solid blue and dashed red lines, respectively. (d) Band alignments of ultra-thin MnF_x structures and other reported single-layers.

increasing temperature. Here, temperature of the 1H-MnF_2, 1T-MnF_2 and MnF_3 crystal structure is increased from 0 K with 2 fs time steps. As shown in Fig. 2(b and d), atomic structure of the 1T-MnF_2 and MnF_3 crystals maintain their stability for high temperatures, while the 1H-MnF_2 crystal is significantly distorted starting from $\sim$200 K.

4 Electronic band structure and possible van der Waals heterostructures

Electronic properties of the 2D MnF_x crystals are investigated through their electronic band structures. In contrast to manganese based dichalcogenide single-layers having metallic character, MnF_x single-layers are semiconductors with varying band gaps (see Fig. 3). 1H-MnF_2 is found to be an indirect band gap semiconductor with a band gap of 3.15 eV. The valence band maximum (VBM) and the conduction band minimum (CBM) are located at the Γ–M interval and the Γ points, respectively. In contrast, 1T-MnF_2 has a direct band gap character whose VBM and CBM are located at the Γ point with a band gap of 3.67 eV. In addition, single-layer MnF_3 is an indirect band gap semiconductor that has a band gap (0.47 eV) much smaller than those of the MnF_2 structures. Its VBM and CBM reside at the Γ and X–S points, respectively. In all three single-layers, the edge of the VBM states is composed of Mn-d and F-p orbitals while the CBM state are dominated by the Mn-d orbitals.

Here, we also investigate the possible heterojunctions of the ultra-thin manganese fluorides with reported single-layers such as MoS_2, WS_2, WSe_2, AlN, GaN, SiC, and GeC.[46,55] Our results show that 1H-MnF_2 has lattice-mismatch of less than 1% with MoS_2, WS_2, and AlN while mismatch of 4% is calculated for GaN and GeC, and 5% for WSe_2. 1T-MnF_2 has lattice-mismatch of 5%, 5%, 2%, 6%, 3%, 7%, and 2% with MoS_2, WS_2, WSe_2, AlN, GaN, SiC, GeC, respectively. Comparative band alignments of these heterojunctions are presented in Fig. 3(d). According to the results, 1H-MnF_2 forms type-I heterojunction with MoS_2, WS_2, WSe_2, AlN, GaN, and SiC while it forms type-III heterojunction with GeC. Type-II heterojunction is also predicted between 1T-MnF_2 and WSe_2, AlN, GaN, SiC. Additionally, 1T-MnF_2 forms type-II heterojunction with GeC and type-I heterojunction with MoS_2 and WS_2 single-layers. Apparently, formation of all three types of heterojunctions are possible with magnetic MnF_2 single layers, therefore these materials are expected to be used in various optoelectronic device applications. In the case of MnF_3, type-III heterojunction with the given materials is predicted. However, due to high lattice mismatch between these single-layers and ultra-thin MnF_3, heterojunction formation is not feasible (Fig. 4).

5 Conclusions

In this study, we have investigated possible manganese fluoride crystals that can be obtained by fluorination of manganese dichalcogenides. Firstly, it is predicted that, similar to that recently performed for conversion of InSe crystals,[10] it is quite possible for the chalcogen atoms of the host lattice to be replaced by fluorine atoms. Total energy optimization and dynamic stability calculations have shown that formation of three novel ultra-thin crystalline manganese fluoride structures is feasible by chemical conversion. It is also revealed by *ab-initio* calculations that these stable ultra-thin crystal structures can form type-I, type-II, and type-III heterojunctions with other ultra-thin materials that have been studied in the literature. Notably, manganese fluorides which do not have ultra-thin phases can be obtained indirectly by fluorination of manganese chalcogenides and this appears to be an effective alternative method for synthesis of new materials needed in rapidly advancing nanotechnology studies.

Conflicts of interest

There are no conflicts to declare.

Acknowledgements

Computational resources were provided by TUBITAK ULAKBIM, High Performance and Grid Computing Center (TR-Grid e-Infrastructure). H. S. Acknowledges financial support from the TUBITAK under the project number 117F095. H. S. acknowledges support from Turkish Academy of Sciences under the GEBIP program.

References

1 H. Wu, W. Zhao and G. Chen, *J. Appl. Polym. Sci.*, 2012, **125**, 3899–3903.
2 A. Abhervé, S. Manas-Valero, M. Clemente-León and E. Coronado, *Chem. Sci.*, 2015, **6**, 4665–4673.
3 R. C. Sinclair, J. L. Suter and P. V. Coveney, *Phys. Chem. Chem. Phys.*, 2019, **21**, 5716–5722.
4 X. Li, W. Cai, J. An, S. Kim, J. Nah, D. Yang, R. Piner, A. Velamakanni, I. Jung and E. Tutuc, *et al.*, *Science*, 2009, **324**, 1312–1314.
5 S. Bae, H. Kim, Y. Lee, X. Xu, J.-S. Park, Y. Zheng, J. Balakrishnan, T. Lei, H. R. Kim and Y. I. Song, *et al.*, *Nat. Nanotechnol.*, 2010, **5**, 574.
6 Y. Zhan, Z. Liu, S. Najmaei, P. M. Ajayan and J. Lou, *Small*, 2012, **8**, 966–971.
7 F.-F. Zhu, W.-J. Chen, Y. Xu, C.-L. Gao, D.-D. Guan, C.-H. Liu, D. Qian, S.-C. Zhang and J.-F. Jia, *Nat. Mater.*, 2015, **14**, 1020–1025.
8 M. Dávila, L. Xian, S. Cahangirov, A. Rubio and G. Le Lay, *New J. Phys.*, 2014, **16**, 095002.
9 J. Chen, M. Duan and G. Chen, *J. Mater. Chem.*, 2012, **22**, 19625–19628.
10 V. Sreepal, M. Yagmurcukardes, K. S. Vasu, D. J. Kelly, S. F. Taylor, V. G. Kravets, Z. Kudrynskyi, Z. D. Kovalyuk, A. Patanè, A. N. Grigorenko, S. J. Haigh, C. Hardacre, L. Eaves, H. Sahin, A. K. Geim, F. M. Peeters and R. R. Nair, *Nano Lett.*, 2019, **19**, 6475–6481.
11 M. Yagmurcukardes, *Phys. Rev. B*, 2019, **100**, 024108.
12 H. Wang, M. Narasaki, Z. Zhang, K. Takahashi, J. Chen and X. Zhang, *Sci. Rep.*, 2020, **10**, 1–10.
13 Z. Mazej, *J. Fluorine Chem.*, 2002, **114**, 75–80.
14 R. Fowler, H. Anderson, J. Hamilton, Jr, W. Burford III, A. Spadetti, S. Bitterlich and I. Litant, *Ind. Eng. Chem. Res.*, 1947, **39**, 343–345.
15 Y. Jiao, F. Ma, C. Zhang, J. Bell, S. Sanvito and A. Du, *Phys. Rev. Lett.*, 2017, **119**, 016403.
16 P. Mondal and W. Domcke, *J. Phys. Chem. A*, 2014, **118**, 3726–3734.
17 M. Poulain, *J. Non-Cryst. Solids*, 1983, **56**, 1–14.
18 J. Lucas, *J. Mater. Sci.*, 1989, **24**, 1–13.
19 K. Rui, Z. Wen, Y. Lu, J. Jin and C. Shen, *Adv. Energy Mater.*, 2015, **5**, 1401716.
20 A. Grenier, A.-G. Porras-Gutierrez, A. Desrues, S. Leclerc, O. J. Borkiewicz, H. Groult and D. Dambournet, *J. Fluorine Chem.*, 2019, **224**, 45–51.
21 T. Tsuboi, P. Silfsten and R. Laiho, *Phys. Rev. B: Condens. Matter Mater. Phys.*, 1991, **43**, 1135.
22 I. Hernández, F. Rodrguez and H. Hochheimer, *Phys. Rev. Lett.*, 2007, **99**, 027403.
23 K. S. Novoselov, A. K. Geim, S. V. Morozov, D. Jiang, Y. Zhang, S. V. Dubonos, I. V. Grigorieva and A. A. Firsov, *Science*, 2004, **306**, 666–669.
24 A. K. Geim and K. S. Novoselov, *Nanoscience and Technology: A Collection of Reviews from Nature Journals*, World Scientific, 2010, pp. 11–19.
25 K. F. Mak, C. Lee, J. Hone, J. Shan and T. F. Heinz, *Phys. Rev. Lett.*, 2010, **105**, 136805.
26 Y. Zhao, X. Luo, H. Li, J. Zhang, P. T. Araujo, C. K. Gan, J. Wu, H. Zhang, S. Y. Quek, M. S. Dresselhaus and X. Qihua, *Nano Lett.*, 2013, **13**, 1007–1015.
27 H. Fang, S. Chuang, T. C. Chang, K. Takei, T. Takahashi and A. Javey, *Nano Lett.*, 2012, **12**, 3788–3792.
28 H. Li, G. Lu, Y. Wang, Z. Yin, C. Cong, Q. He, L. Wang, F. Ding, T. Yu and H. Zhang, *Small*, 2013, **9**, 1974–1981.
29 G. W. Mudd, S. A. Svatek, T. Ren, A. Patanè, O. Makarovsky, L. Eaves, P. H. Beton, Z. D. Kovalyuk, G. V. Lashkarev, Z. R. Kudrynskyi and A. I. Dmitriev, *Adv. Mater.*, 2013, **25**, 5714–5718.
30 B. Huang, G. Clark, E. Navarro-Moratalla, D. R. Klein, R. Cheng, K. L. Seyler, D. Zhong, E. Schmidgall, M. A. McGuire, D. H. Cobden, W. Yao, D. Xiao, P. Jarillo-Herrero and X. Xu, *Nature*, 2017, **546**, 270.
31 T. Kong, K. Stolze, E. I. Timmons, J. Tao, D. Ni, S. Guo, Z. Yang, R. Prozorov and R. J. Cava, *Adv. Mater.*, 2019, **31**, 1808074.
32 M. Baskurt, I. Eren, M. Yagmurcukardes and H. Sahin, *Appl. Surf. Sci.*, 2020, **508**, 144937.
33 S. Tian, J.-F. Zhang, C. Li, T. Ying, S. Li, X. Zhang, K. Liu and H. Lei, *J. Am. Chem. Soc.*, 2019, **141**, 5326–5333.
34 D. J. O'Hara, T. Zhu, A. H. Trout, A. S. Ahmed, Y. K. Luo, C. H. Lee, M. R. Brenner, S. Rajan, J. A. Gupta and D. W. McComb, *et al.*, *Nano Lett.*, 2018, **18**, 3125–3131.
35 G. Kresse and J. Hafner, *Phys. Rev. B: Condens. Matter Mater. Phys.*, 1993, **47**, 558.
36 G. Kresse and J. Furthmüller, *Phys. Rev. B: Condens. Matter Mater. Phys.*, 1996, **54**, 11169.
37 P. E. Blöchl, *Phys. Rev. B: Condens. Matter Mater. Phys.*, 1994, **50**, 17953–17979.
38 J. P. Perdew, K. Burke and M. Ernzerhof, *Phys. Rev. Lett.*, 1996, **77**, 3865–3868.
39 S. Dudarev, G. Botton, S. Savrasov, C. Humphreys and A. Sutton, *Phys. Rev. B: Condens. Matter Mater. Phys.*, 1998, **57**, 1505.
40 A. Jain, G. Hautier, S. P. Ong, C. J. Moore, C. C. Fischer, K. A. Persson and G. Ceder, *Phys. Rev. B: Condens. Matter Mater. Phys.*, 2011, **84**, 045115.
41 S. Grimme, S. Ehrlich and L. Goerigk, *J. Comput. Chem.*, 2011, **32**, 1456–1465.
42 D. Alfe, *Comput. Phys. Commun.*, 2009, **180**, 2622–2633.
43 G. Henkelman, A. Arnaldsson and H. Jónsson, *Comput. Mater. Sci.*, 2006, **36**, 354–360.
44 A. Fonari and S. Stauffer, vasp raman.py, https://github.com/raman-sc/VASP/, 2013.
45 M. Yagmurcukardes, F. M. Peeters and H. Sahin, *Phys. Rev. B*, 2018, **98**, 085431.
46 C. Ataca, H. Sahin and S. Ciraci, *J. Phys. Chem. C*, 2012, **116**, 8983–8999.
47 I. Eren, F. Iyikanat and H. Sahin, *Phys. Chem. Chem. Phys.*, 2019, **21**, 16718–16725.
48 W. Chen, J.-M. Zhang, Y.-Z. Nie, Q.-L. Xia and G.-H. Guo, *J. Phys. Chem. Solids*, 2020, **143**, 109489.

49 M. Yagmurcukardes, R. Senger, F. Peeters and H. Sahin, *Phys. Rev. B*, 2016, **94**, 245407.
50 M. Yagmurcukardes, C. Bacaksiz, E. Unsal, B. Akbali, R. Senger and H. Sahin, *Phys. Rev. B*, 2018, **97**, 115427.
51 Y. Li, S. Luo, M.-C. Yang, R. Liang and C. Zeng, *Adv. Funct. Mater.*, 2016, **26**, 2900–2908.
52 L. Y. W. Loh, U. Gupta, Y. Wang, C. C. Foo, J. Zhu and W. F. Lu, *Adv. Eng. Mater.*, 2021, 2001082.
53 Z. W. Ulissi, A. Govind Rajan and M. S. Strano, *ACS Nano*, 2016, **10**, 7542–7549.
54 A. Alderson, J. Rasburn, S. Ameer-Beg, P. G. Mullarkey, W. Perrie and K. E. Evans, *Ind. Eng. Chem. Res.*, 2000, **39**, 654–665.
55 H. Sahin, S. Cahangirov, M. Topsakal, E. Bekaroglu, E. Akturk, R. T. Senger and S. Ciraci, *Phys. Rev. B: Condens. Matter Mater. Phys.*, 2009, **80**, 155453.